

Interface reconstruction in superconducting $\text{CaCuO}_2/\text{SrTiO}_3$ superlattices: A hard x-ray photoelectron spectroscopy study

C. Aruta,^{1,*} C. Schlueter,² T.-L. Lee,³ D. Di Castro,⁴ D. Innocenti,⁴ A. Tebano,⁴ J. Zegenhagen,² and G. Balestrino⁴

¹*CNR-SPIN, Dipartimento di Scienze Fisiche, Via Cintia, Monte S. Angelo, 80126 Napoli, Italy*

²*ESRF, 6 rue Jules Horowitz, BP 220, 38043 Grenoble, CEDEX 9, France*

³*Diamond Light Source Ltd, Harwell Science and Innovation Campus, Didcot, OX11 0DE, UK*

⁴*CNR-SPIN and Dipartimento di Ingegneria Civile ed Ingegneria Informatica, Università di Roma Tor Vergata, Via del Politecnico 1, 00133 Roma, Italy*

(Dated: June 16, 2021)

Here we report about the interface reconstruction in the recently discovered superconducting artificial superlattices based on insulating CaCuO_2 and SrTiO_3 blocks. Hard x-ray photoelectron spectroscopy shows that the valence bands alignment prevents any electronic reconstruction by direct charge transfer between the two blocks. We demonstrate that the electrostatic built-in potential is suppressed by oxygen redistribution in the alkaline earth interface planes. By using highly oxidizing growth conditions, the oxygen coordination in the reconstructed interfaces may be increased, resulting in the hole doping of the cuprate block and thus in the appearance of superconductivity.

I. INTRODUCTION

Reconstruction phenomena at the interfaces between complex oxides result in novel metallic, magnetic and superconducting 2D phases¹. In the case of cuprate interfaces, charge redistribution involving CuO_2 planes may give rise to high temperature superconductivity. In common high temperature superconductors (HTS) the virtual separation between the charge reservoir (CR) and the infinite layer (IL) blocks can be regarded as a native interface. The CR block is charge unbalanced by cation substitution or oxygen deficiency and charge carriers are transferred to the IL block giving rise to superconductivity in the CuO_2 planes. Such a structural paradigm has lead investigators to mimic the standard stacking of HTS compounds by layer-by-layer deposition techniques. Two different layers, neither of which superconducting on their own, act as the IL and the CR blocks, respectively, to create the conceptually simplest case of a cuprate HTS. Understanding charge redistribution at the interface of such artificial heterostructures should be very useful for unveiling the nature of high transition temperature superconductivity and may open new routes for engineering novel HTSs.

In this context, superconductivity was reported in heterostructures consisting of an insulating and a metallic cuprate, namely CaCuO_2 (CCO) and BaCuO_2 (BCO).^{2,3} CCO has the IL structure where the CuO_2 planes are separated by bare Ca atoms. The BCO, which has a more complex structure including extra apical oxygen ions, behaves as the CR block. In CCO/BCO superlattices (SLs), the redistribution of the hole doping between the in-plane and the out-of-plane orbitals of $\text{Cu } 3d(e_g)$ was proven by x-ray absorption measurements (XAS) at the $\text{Cu } L$ -edge.⁴ The transition temperature T_c followed a typical bell-shape dependence on the number n of CuO_2 planes in the CCO block. The highest T_c (80 K) was reported for $n = 3$.⁵ Successively, superconductivity has been also reported in bilayers con-

sisting of the insulator La_2CuO_4 (LCO) and the metal $\text{La}_{1.55}\text{Sr}_{0.45}\text{CuO}_4$ (LSCO).⁶ A highest T_c of about 30 K was obtained and the superconductivity was identified to originate from an interface layer of about 1 - 2 unit cells in thickness.⁷ More recently, superconductivity was found in $\text{CaCuO}_2/\text{SrTiO}_3$ (CCO/STO) SLs grown under strongly oxidizing conditions with a maximum T_c of about 40K.⁸ The role of the extra oxygen at the interfaces, which thus act as charge reservoir for the CCO block, was envisaged by the presence of $\text{Cu } 3d(e_g)$ holes with out-of-plane orbital symmetry, observed by XAS measurements.⁸ Similarly, interfacial $\text{Cu } 3d_{3z^2-r^2}$ orbitals of CCO were also observed in $\text{La}_{1-x}\text{Sr}_x\text{MnO}_3/\text{CCO}$ SLs.⁹ Accordingly, first-principles total energy calculations, reported in literature, demonstrated that out-of-plane chain-type CuO is formed at the interface between the IL ACuO_2 ($A = \text{Ca}, \text{Sr}, \text{Ba}$) and the STO substrate.¹⁰ This chain acts as a bridge between the IL film and the STO and, thus, possibly drives the orbital reconstruction.

In the present work we study CCO/STO SLs by hard x-ray photoelectron spectroscopy (HAXPES), which has been demonstrated to be a powerful technique for the study of complex oxides heterostructures¹¹. Our HAXPES study shows an enhanced oxygen coordination at the interfaces, in agreement with previous suggestions⁸ and theoretical findings.¹⁰ Moreover, we show that the band alignment after interface reconstruction prevents the direct charge transfer between the CCO and STO. We demonstrate that the built-in electrostatic potential, arising at the polar/non-polar CCO/STO interface, similarly to LAO/STO interface, can be suppressed by oxygen redistribution at the interface, giving rise to different oxygen coordinations. The resulting compositional roughening is fundamental for the hole doping of the CuO_2 planes, which may open a new route to the design of superconducting heterostructures.

II. EXPERIMENTAL

The CCO/STO SLs were grown on A-site terminated $NdGaO_3(110)$ (NGO) substrates by pulsed laser deposition, following the procedure described in ref. 8. Two different kinds of CCO/STO SLs, made by 20 repetitions of the supercell constituted by 3-4 unit cells (uc) of CCO and 2 uc of STO, were studied by HAXPES: (i) non-superconducting (non-SC) samples and (ii) superconducting (SC) samples with maximum zero resistance temperature $T_c \approx 40K$. The non-SC samples were grown in a weakly oxidizing atmosphere (oxygen pressure lower than 0.1 mbar) and the SC samples were grown in a highly oxidizing atmosphere (oxygen with 12% ozone at a pressure of about 1 mbar) and subsequently rapidly quenched to room temperature in 1 bar of oxygen pressure. The temperature dependence of the resistance for these two kinds of SLs is reported in Fig. 1(a). Further details on the transport properties are reported in ref. 8. As references we measured a bare STO substrate slightly oxygen reduced in order to increase its conductivity and thus to avoid charging effects, and a 10 nm thick CCO film on NGO, prepared under conditions identical to those for the SC SLs. Room temperature HAXPES measurements were performed at the ID32 beamline of the European Synchrotron Radiation Facility in Grenoble (France) using a PHOIBOS 225 HV analyzer (SPECS, Berlin, Germany) pointing in the polarization direction of the photon beam.¹⁷ Excitation energies from 2.8 keV (inelastic mean free path $\lambda \approx 30\text{\AA}$) to 5.95 keV ($\lambda \approx 50\text{\AA}$) were used and the electron emission angle with respect to the surface was varied from 15° to 70° to change the probing depth. The overall instrumental resolution was better than about 400meV (the best was about 200meV at 5.95keV), as determined by the width of the Fermi edge of a Au reference sample. The energy calibration was performed by measuring the $Au 4f_{7/2}$ core level peak during the same experimental run. For the analysis of the HAXPES spectra a Shirley function was assumed for background subtraction and a multicomponent deconvolution procedure, using mixed Gaussian/Lorentzian line shapes to extract the exact line positions and intensities. The coefficient of determination of the final fit resulted always close to one. In the case of $Cu 2p_{3/2}$ core level the number of components was chosen in agreement with the theoretical works of refs. 18,19. In the case of $Sr 3d$, $Ca 2p$ and $Ti 2p_{3/2}$ core levels we used the minimum number of components compatible with the doublets of the spin-orbit splitting. Indeed, the spin-orbit coupling splits the $3d$ states into $j=3/2$ and $5/2$, and the $2p$ states into $j=1/2$ and $3/2$. Therefore, we used a number of doublets to fit the $Sr 3d$ and $Ca 2p$ core level spectra, while we used a number of peaks to fit only the $2p_{3/2}$ spectrum of Ti and Cu , being well separated in energy from the $2p_{1/2}$ spectrum. For the spin-orbit ratio we used the degeneracy ratios 2:3 and 1:2 for $Sr 3d$ and $Ca 2p$, respectively. The spin-orbit splitting was set to the values reported in the database of National Institute of Standard and

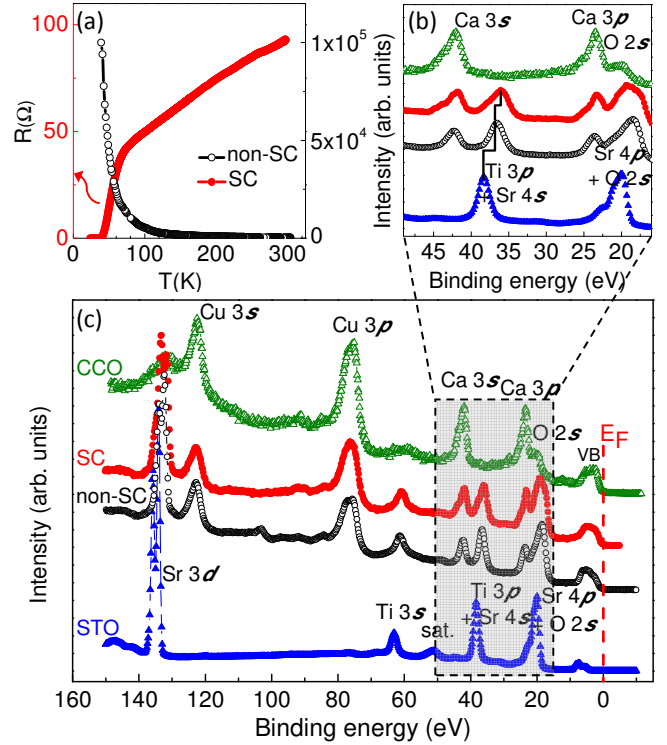


FIG. 1: (Color online) (a) Temperature dependence of the resistance of the SC SL (close red circles) and non-SC SL (open black circles). (b) Magnified portion of the spectra of the bottom panel between 49 and 16 eV. (c) Core level spectra from 150 to -10 eV binding energy of the non-SC SL (open black circles), the SC SL (close red circles), the STO substrate (close blue triangles) and the CCO film (open green triangles) grown in the same conditions of the SC SL. Measurements were performed at 2.8 keV excitation energy and with an electron emission angle of 70° .

Technology (NIST).²⁰ The Full Width at Half Maximum (FWHM) of the fit components is fixed for each $Sr 3d$, $Ca 2p$ and $Ti 2p_{3/2}$ core-level spectrum, as reported in the next section.

III. RESULTS

A. Band alignment

The low binding energy core levels spectra of SC and non-SC SLs are presented in Fig.1(b) and (c), together with those of the CCO film and the STO substrate used as references. In the SC spectrum a shift of about 1.5-2.0 eV of the Sr and Ti core levels toward lower energies with respect to STO can be observed, as emphasized in Fig.1 (b). On the contrary, the shifts of the Ca and Cu core levels with respect to CCO are negligible. A similar, but minor, behavior can be observed for the non-SC SL. The difference between the shift of the core levels of the SC and non-SC samples can be also observed

in the spectra of Figs. 4-6 and evidenced by the peak positions reported in Tables I-IV. As a matter of fact, we are dealing with an upward core level shift of the STO peaks relative to the CCO peaks, which also leads to the band alignment between CCO and STO blocks after the interfacial reconstruction in the SLs (see Fig. 2 (c) and (d)). We used the shallow core levels (E_{cl}) of Fig. 1 (c) and the valence band (VB) maximum (E_v) in the STO and CCO reference samples of Fig.2(a), to calculate the VB offset $\Delta E_v = E_v^{CCO} - E_v^{STO}$ for both the SC and the non-SC SLs as in the following:^{21,22}

$$\Delta E_v = (E_{cl}^{CCO} - E_{cl}^{STO})_{SL} - [(E_{cl}^{STO} - E_v^{STO}) - (E_{cl}^{CCO} - E_v^{CCO})]$$

where the subscript SL indicates that E_{cl}^{CCO} and E_{cl}^{STO} are the values in the SL. Using different pairs of the core levels *Sr* 3d, *Cu* 3s, *Ti* 3s and *Ca* 3s, we obtained an average ΔE_v value of 1.7 ± 0.2 eV and 1.3 ± 0.2 eV for the non-SC and the SC sample, respectively. The origin of the chemical shift and of the resulting band alignment in the SLs is not obvious. The band offset, and therefore the chemical shift, depends on the alignment of the chemical potentials of the two constituent blocks. After the interface reconstruction, the energy shift of the photoelectrons can depend not only on the charge transfer, but also on other effects related to interface dipole, valence, coordination or strength of bonds. The exact origin of the chemical shift and of the band alignment is beyond the scope of this paper. However, we will examine the consequence of these experimental findings: as described by Yunoki and coworkers,²³ in order to have charge transfer between insulating CCO and STO bands, after interface reconstruction, the top of the valence band of CCO (STO) should lie above the bottom of the conduction band of STO (CCO). As a matter of fact, under the alignment conditions shown in Fig.2(c)-(d) we do not expect any direct charge transfer between CCO and STO bands. Therefore the doping, which gives rise to superconductivity in our SLs, must have a different explanation. In the next section we discuss the possible effects of the polarity of the atomic planes of the CCO on the interfacial reconstruction.

B. Oxygen redistribution

1. Suppression of the interface electrostatic potential

The CCO/STO interface under study shows some interesting similarities with the widely studied *LaAlO₃/SrTiO₃* (LAO/STO) system.¹² The polarity of the LAO film on the non-polar STO gives rise to a built-in electrostatic potential at the LAO/STO interface which diverges with the LAO film thickness. Different mechanisms have been proposed for the suppression of this divergent potential, including compositional roughening of the interface, electronic reconstruction, elements interdiffusion and buckling at the interface.¹³⁻¹⁶ In ref.13 it was suggested that the suppression mechanism in

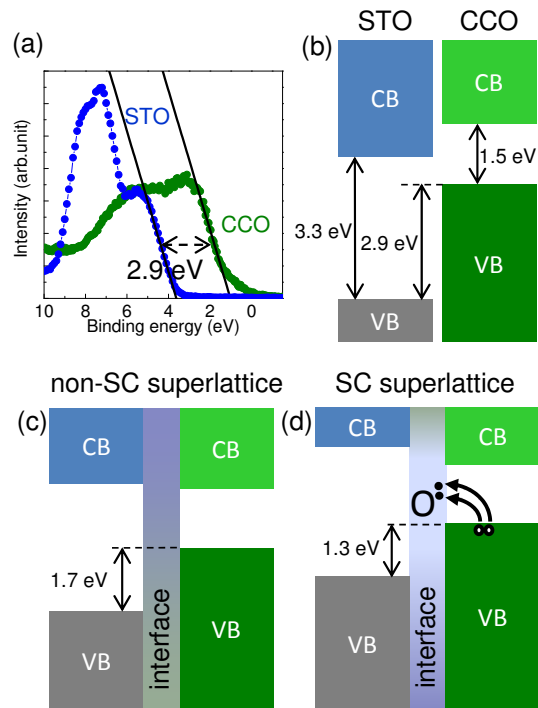


FIG. 2: (Color online)(a) Valence band spectra for the CCO and the STO, together with the linear extrapolation of the leading edge of the VB spectra. (b)-(d) Schematic diagram of the valence and conducting bands for the uncoupled CCO and STO reference samples shown in (b), for the non-SC SL shown in (c) and for the SC SL shown in (d). Excess oxygen at the interface of SC SL induces two holes in the VB of CCO for each extra oxygen ion (see panel (d)), to preserve the charge neutrality of the system. In all panels (b)-(d) we assume the bulk band gap values for the STO (3.3 eV) and the CCO (1.5 eV) layers.^{24,25}

LAO/STO depends on the termination of the STO substrate. A *TiO₂* termination can lead to an electronic reconstruction that involves charge transfer of half an electron per unit cell from the LAO layer to the *TiO₂* interfacial plane, resulting in a metallic interface.¹² A *SrO* termination, on the other hand, requires an atomic reconstruction that removes half oxygen ion per unit cell from the *SrO* interfacial plane, leading to an insulating interface. Similarly, in the CCO/STO system, the (001) planes of CCO consist of *Ca* and *CuO₂* layers with formal charges of $+2e$ and $-2e$, respectively, where e is the elementary charge. Fig. 3(a) shows an atomically abrupt, unreconstructed interface between the polar CCO and the non-polar STO layers, leading to a built-in electrostatic potential that increases with the CCO thickness and with the number of repetitions of the CCO block. This is similar to the case of the polar/non-polar LAO/STO interface. However, the built-in potential in CCO/STO is expected to be twice as large as that in LAO/STO because the uncompensated charge of each atomic plane in CCO is $\pm 2e$ per unit cell, as mentioned above, compared to $\pm 1e$ for LAO/STO. In the case of

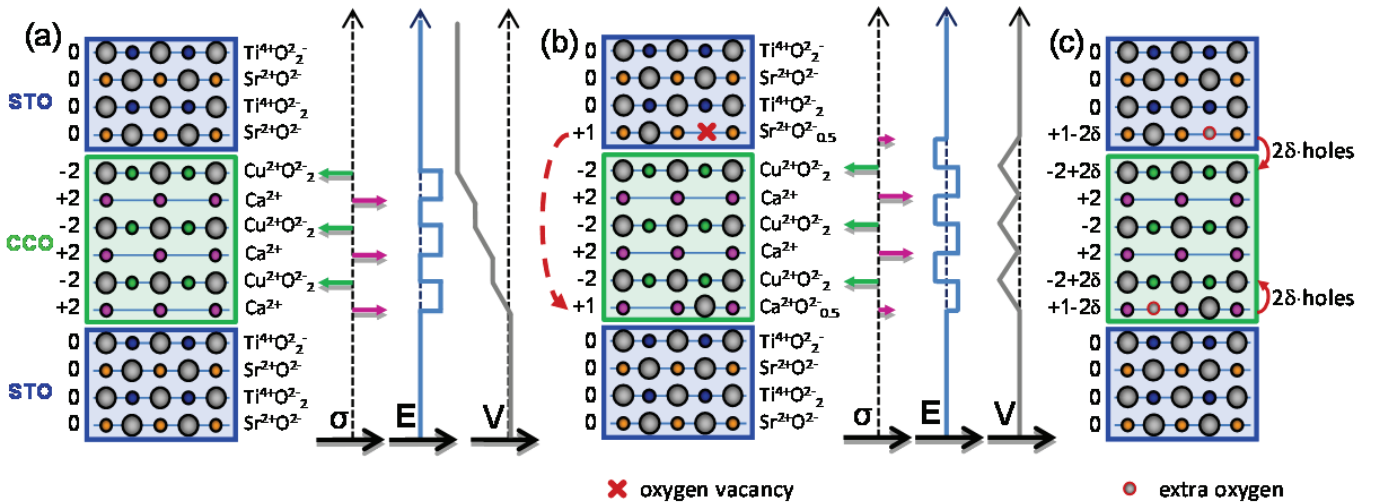


FIG. 3: (Color online) Sketch of CCO/STO SLs with neutral (001) planes in STO and alternating net charges (σ) in CCO. The electric field (E) and the resulting electrostatic potential V are also shown. (a) Unreconstructed interfaces where the electrostatic potential diverges with thickness. (b) Reconstructed interfaces where the possible suppression of the built-in potential occurs by an ionic mechanism: half oxygen atom per uc is transferred from the SrO plane to the Ca plane. (c) The insertion of an amount δ of extra oxygen at interfaces slightly decreases the positive net charge by 2δ at CaO and SrO planes, which can be compensated by 2δ holes in the adjacent CuO_2 planes.

LAO/STO the buildup of the electrostatic potential was estimated in the range of 0.6 - 0.9 V/uc^{26,27}. We thus expect this value to roughly double for CCO/STO, if we assume that the dielectric constant of CCO is about the same as for LAO. The expected steeply increasing potential in CCO/STO of Fig. 3(a) should result in a severe broadening of the core level spectra. Indeed, they would be the convolution of differently shifted spectra from atomic planes at several depths, thus at different electrostatic potential. By varying the emission angle it is possible to largely change the probing depth (see Fig. 4 (a)). We therefore collected spectra at 15° and 70°. At the 15° emission angle the Sr 3d intensity comes mostly from the topmost STO layer, while at 70°, the escape depth of the emitted electrons is estimated to be 3.6 times larger and thus the top three to four STO layers all contribute to the intensity. Therefore, in the presence of an unquenched built-in potential, the Sr spectrum recorded at 70° should be much broader than the one recorded at 15°. The Sr 3d core level spectra of a SC SL shown in Fig.4(b) and (c) for the 15° and 70° emission angles, respectively, contain multiple peaks which were deconvoluted using the fit procedure. The resulting positions, areas, and widths of each peak are summarized in Table I. In fact, it can be noticed that, although the Sr 3d of the SL splits into two doublets, whose origin will be discussed later, the peak width is independent on the emission angle. This finding clearly shows that the built-in electrostatic potential is suppressed even for a three unit cells thick CCO block. A simplified mechanism for the suppression of the electrostatic potential can be based on the oxygen redistribution, as shown in Fig. 3(b): half oxygen ion moves

from the SrO plane to the Ca plane, so that the electric field at both ends of the CCO block is eliminated. Even though we might expect a more complex mechanism, the oxygen compositional roughening, resulting from the proposed model, is supported by the presence of additional peaks/doublets in all the measured core levels spectra.

TABLE I: Fit results of the Sr 3d spectra shown in Fig. 4. Due to the small spin-orbit splitting, both peaks of the doublet ($j=3/2, 5/2$) are considered. The spin-orbit splitting was fixed at 1.8 eV and the intensity ratio to 2:3, in agreement with the degeneracy value. Only the energy position for the $3d_{5/2}$ is given in the Table.

		Sr 3d		width (eV)
		Doublet		
		1	2	
SC 15°	pos (eV)	131.5	132.9	1.7
	area (%)	68	32	
SC 70°	pos (eV)	131.4	133.0	1.7
	area (%)	70	30	
non-SC 70°	pos (eV)	132.2	133.8	1.5
	area (%)	90	10	

2. Additional components in Sr 3d, Ca 2p and Ti 2p_{3/2}

In the perovskite structure of STO, the Sr^{2+} is 12-fold cuboctahedrally coordinated with oxygen ions. Similarly, in the ideal infinite layers structure, the Ca^{2+} ions

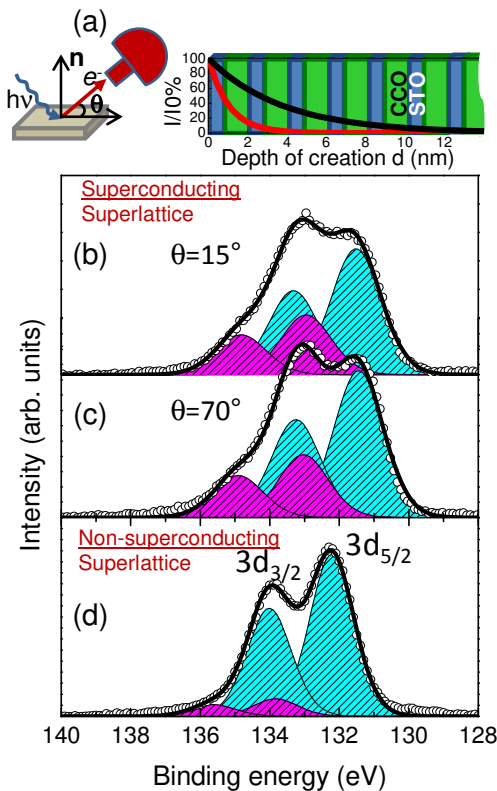


FIG. 4: (Color online) (a) Schematic of the experimental geometry and probability of electron escape without loss $I/I_0 = \exp(-d/\lambda \sin\theta)$, where λ is the inelastic mean free path ($\lambda \approx 4nm$) and θ is the emission angle. The probability curves are superimposed to the schematic of the CCO/STO SL: red curve is for $\theta = 15^\circ$ and black curve is for $\theta = 70^\circ$. (b) $Sr\ 3d$ core level HAXPES spectra of the SC SL measured at an emission angle of 15° . (c) $Sr\ 3d$ core level spectra of the same sample measured at an emission angle of 70° . (d) $Sr\ 3d$ core level spectra of the non-SC SL measured at an emission angle of 70° . All the measurements were performed at 2.8 keV excitation energy. In (b)-(d) panels, experimental data (open circles) are compared with the fit curves (straight black line). The fit curves are obtained as the convolution of the couple of doublets reported in the figures as filled areas (cyan and magenta) under curves.

occupy a single site coordinated with 8 oxygen ions (in the infinite layer structure the 4 oxygen ions in the Ca plane are missed relative to the perovskite structure). As a consequence, both the $Sr\ 3d$ (in the perovskite structure) and the $Ca\ 2p$ (in the ideal IL structure) core levels give rise to a single well defined doublet in the HAXPES spectrum. The doublets occur because of the spin-orbit coupling which splits the core initial states into $j=3/2, 5/2$ for $Sr\ 3d$ (Fig. 4(b)-(d)) and $j=1/2, 3/2$ for $Ca\ 2p$ (Fig.5 (c) and (d)). In the case when no reconstruction occurs in the CCO/STO superlattice, the Ca and Sr ions should maintain the same coordination as in the parent compounds without additional core level peaks. In fact, both the $Sr\ 3d$ and the $Ca\ 2p$ core levels show several components, more pronounced in the SC (Fig. 4(b)-(c)

and Fig. 5(c)) compared to the non-SC SL ((Fig. 4(d) and Fig. 5(d)). The fit results for the $Ca\ 2p$ core levels are reported in Table II. While in the case of the non-SC SL we used two doublets, three doublets were necessary in the case of the SC SL to obtain a reliable fit with a coefficient of determination close to one. The

TABLE II: Fit results of the $Ca\ 2p$ spectra shown in Fig. 5(c) and (d). Due to the small spin-orbit splitting, both peaks of the doublet ($j=1/2, 3/2$) are considered. The spin-orbit splitting was fixed at 3.5 eV and the intensity ratio to 1:2, in agreement with the degeneracy value. Only the energy position for the $2p_{3/2}$ is given in the Table.

		Ca 2p			width (eV)
		Doublet			
		1	2	3	
SC	pos(eV)	344.5	345.6	346.9	1.3
	area (%)	63	23	14	
non-SC	pos (eV)	344.6	345.7		1.3
	area (%)	78	22		

additional components used for the fit, both in the case of $Sr\ 3d$ and of $Ca\ 2p$, can be explained in terms of Sr/Ca site having different oxygen coordination. We ascribe such an effect to the presence at the interfaces of non equivalent Sr ions with 12-N oxygen coordination and non-equivalent Ca ions with 8+N oxygen coordination, with N ranging from 1 to 4. Similarly, the $Ti\ 2p_{3/2}$ core levels were successfully fitted with two peaks (Fig.5 (a) and (b)). We take into consideration only the $2p_{3/2}$, as the $Ti\ 2p_{1/2}$ - $Ti\ 2p_{3/2}$ spin-orbit splitting is $\simeq 6$ eV. The fit results are reported in Table III. The presence of additional components in all the core levels spectra is in agreement with the occurrence of oxygen redistribution, schematically depicted in Fig. 3(b), needed to suppress the electrostatic built-in potential. In addition, the shape of the spectra of all the core levels strongly depends on the oxidation conditions used during the film growth. Such a finding demonstrates that the oxygen distribution plays also a crucial role for the appearance of superconductivity. Indeed, consistently with stronger oxidation, in the SC sample the relative intensity of the additional components, at the higher binding energy at the $Ti\ 2p$ and $Sr\ 3d$, is larger and one more doublet appears at the $Ca\ 2p$ core level (see Fig. 4 and 5). Additionally, in the case of strongly oxidizing conditions, some extra oxygen can enter in the interface CaO and SrO planes that, thus, behave as charge reservoir for the IL block. This is schematically shown in Fig. 3(c). The slight consequent decrease of the positive charge at the interfaces is compensated by the introduction of positive charge (holes) in the CuO_2 interface planes to preserve charge neutrality: overall the suppression of the polar catastrophe is preserved.

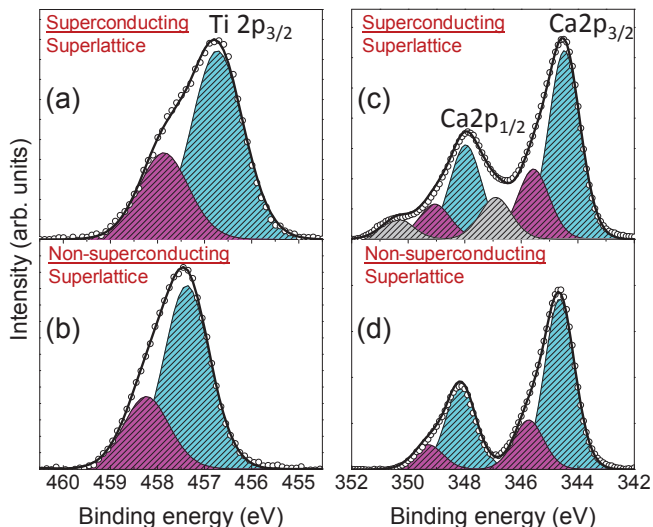


FIG. 5: (Color online) $Ti\ 2p_{3/2}$ core level HAXPES spectra for (a) SC and (b) non-SC SLs. $Ca\ 2p$ core level spectra for (c) SC and (d) non-SC SLs. Measurements were performed at 2.8 keV excitation energy and an emission angle of 70° . In all panels, experimental data (open circles) are compared with the fit results (straight black line), obtained as the envelope of the fit curve components reported in the figures as filled areas (cyan, magenta and grey) under curves.

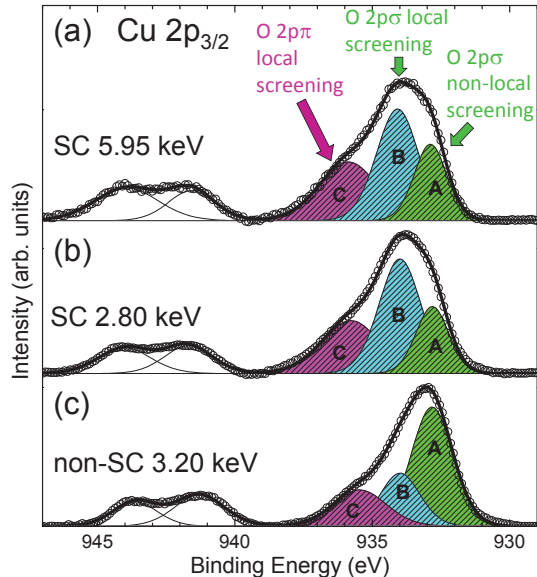


FIG. 6: (Color online) $Cu\ 2p_{3/2}$ spectra of a SC sample at two different excitation energy, 5.95 keV (a) and 2.8 keV (b) and of a non-SC sample at an intermediate excitation energy, 3.2 keV (c). Measurements were performed at an emission angle of 70° . In all panels, experimental data (open circles) are compared with the fit results (straight black line), obtained as the envelope of the fit curve components A, B and C.

TABLE III: Fit results of the $Ti\ 2p_{3/2}$ spectra shown in Fig.5(a) and (b)

		Ti $2p_{3/2}$ Peak		width (eV)
		1	2	
SC	pos (eV)	456.7	457.9	1.3
	area (%)	68	32	
non-SC	pos (eV)	457.4	458.2	1.2
	area (%)	72	28	

3. Screening features in $Cu\ 2p_{3/2}$

$Cu\ 2p$ core level spectra for the SC and non-SC SLs are reported in Fig. 6. The $Cu\ 2p$ spectra have a large spin-orbit splitting between the $Cu\ 2p_{3/2}$ and $Cu\ 2p_{1/2}$ (not shown) components with asymmetrical peak shapes. In addition each component is accompanied by a pronounced shake-up satellite peak at higher binding energies (between about 940 and 945 eV). We will focus on the $Cu\ 2p_{3/2}$ only. Fig.6 shows the $Cu\ 2p_{3/2}$ spectra for a SC sample measured at an excitation energy of 5.95 keV (inelastic mean free path $\lambda \approx 50\text{\AA}$), for the same sample measured at 2.80 keV ($\lambda \approx 30\text{\AA}$) and for a non-SC sample measured at 3.2 keV ($\lambda \approx 34\text{\AA}$). The interpretation of the $Cu\ 2p$ spectrum is less straightforward due to its dependence on the dynamics of valence electrons. In fact, the core level photoemission process leads to a final state with a hole in the $2p$ core orbital of a Cu site. The resulting positive charge is screened by valence electrons, predominantly from $Cu\ 3d_{x^2-y^2}$ and $O\ 2p_{x,y}$ orbitals, which modifies the kinetic energy and thus seemingly the binding energy of the emitted photoelectrons.³⁰ The contribution of these screening processes to the final state determines the detailed form of the experimental spectrum. In fact, Fig. 6 shows that the $Cu\ 2p_{3/2}$ peak shape is highly asymmetric. This is particularly evident for the SC SL spectrum at 5.95 keV excitation energy. Following the work by van Veenendaal,¹⁸ the core hole can be screened by electrons from the oxygen atoms surrounding the site with the core-hole (feature B), known as local screening process. On the other hand, the core hole can be screened by electrons from the ligand atoms surrounding a neighboring CuO_4 plaquette (feature A), known as non-local screening. It has been reported that local and non-local screening effects give rise to two different spectral features, about 1-1.5 eV apart.¹⁸ Non-local screening features can be observed using hard x-rays in several transition metal oxides,³¹⁻³⁴ whereas it is very weak for common laboratory soft x-ray sources.^{31,32} Accordingly, Fig. 6(a) and (b) show that this feature becomes more evident when using higher excitation energy. Based on the theoretical work of Okada and Kotani,¹⁹ we used an additional component to fit our data (feature C) at about 2 eV higher binding energy than feature B. It was reported that an higher binding energy component, as feature C,

arises when the contribution of out-of-plane orbitals to the local screening is included in the calculations.¹⁹ The presence of apical oxygen at the interfaces was already envisaged in non-SC CCO/STO samples studied by resonant inelastic x-ray scattering³⁵ and in SC CCO/STO samples studied by XAS.⁸ The fit results of $Cu\ 2p_{3/2}$ core level assuming three screening components are reported in table IV. For a direct comparison between the SC and the non-SC SLs, we used three components to fit all the data, keeping fixed the binding energy difference between A and B. The comparison of the $Cu\ 2p_{3/2}$ spectrum of the SC sample with the $Cu\ 2p_{3/2}$ spectrum of the non-SC sample taken at the intermediate excitation energy of 3.2 keV (Fig. 6(c)) shows some differences, which deserve careful discussion. In cuprates the non-local screening gives rise to new Zhang-Rice singlets (ZRS) on the neighboring CuO_4 plaquette. The increase of the local screening at expenses of the non-local screening channel can be observed by comparing the relative intensity of local and non-local screening features (B/A) in the SC sample (Fig.6(a) and (b)) with B/A in the non-SC sample (Fig.6(c)). This result is in agreement with the hole doping of the SC sample. Indeed, ZRS are already present in the hole-doped systems and the non-local screening is less effective, because such screening should form new states with ZRS. As a consequence, the non-local screening is compensated by an increased screening of the core-hole by local electrons (local screening). Moreover, the relative weight of feature C to the whole spectrum is higher in the SC sample, because of the larger concentration of oxygen ions at the interface, which are apical for the copper atoms.

TABLE IV: Fit results of the $Cu\ 2p_{3/2}$ spectra shown in Fig.6.

		Cu $2p_{3/2}$		
		Component		
		A	B	C
SC 5.95 keV	pos(eV)	932.9	934.1	935.9
	width (eV)	1.4	1.8	2.5
	area (%)	33	34	33
SC 2.80 keV	pos(eV)	932.8	934.0	935.8
	width (eV)	1.4	1.8	2.5
	area (%)	33	34	33
non-SC 3.20 keV	pos(eV)	932.8	934.0	935.5
	width (eV)	1.8	1.7	2.3
	area (%)	55	23	22

IV. DISCUSSION

The schematic drawing of Fig.3 summarizes the interface reconstruction inferred by our experimental results. The suppression mechanism of the interface electrostatic potential of Fig.3(a), cannot be based on a purely electronic reconstruction involving exclusively charge trans-

fer between the CCO and STO blocks. Indeed, the band alignment of Fig. 2 (c) and (d), calculated by the core levels shifts of Fig.1, rules out the possibility of any direct charge transfer between CCO and STO bands.²³ Several examples for suppression of a built-in potential are reported in literature, based on an atomic rearrangement at the interface, as in the case of the $GaAs/Ge$ interface and the LAO/STO interface.^{28,29} In the present case, a possible mechanism for the suppression of the interfacial electrostatic potential can be based on a pure ionic mechanism, similar to the case of the interface between SrO terminated STO and LAO, where the SrO interface plane is depleted of half oxygen ion per uc.¹³ The oxygen redistribution in the case of our CCO/STO SLs is schematically reported in Fig. 3(b). Both the Ca and Sr interface planes may accommodate a variable content of oxygen ions, although probably not at the same extent: $CuO_2 - CaO_x - TiO_2$ and $CuO_2 - SrO_y - TiO_2$. If we assume for sake of simplicity $x \approx y \approx 0.5$ the increasing built-in potential is suppressed, as shown in Fig.3(b). When the film deposition is performed at high oxidizing condition, excess oxygen is introduced at the interfaces and the charge neutrality is preserved by leaving two holes in the valence band of CCO for each extra oxygen ion. The evidence of the hole doping by $Cu\ 2p_{3/2}$ core level HAXPES spectra confirms what previously reported in ref. 8, by Hall effect and XAS measurements. The doping mechanism schematized in Fig. 3(c) preserves the suppression of the electrostatic potential, as demonstrated by the core level peak width which is independent on the measurement probing depth (Fig. 4(b) and (c)). The average electrostatic potential of the CCO block is expected to be similar in the SC and the non-SC samples. However different local charges can be formed causing internal electric fields. In addition, the chemical shift also depends on the chemical and structural environment of the atoms in a non trivial way, determining the different core levels shifts experimentally observed in the SC and the non-SC samples (Fig.1(b)). As a consequence, the derived band alignments are also different. Further investigation is required to better clarify the different shift between the SC and non-SC SLs. Nevertheless, in both type of SLs, the derived band alignment supports the interface reconstruction by the oxygen rearrangement. The resulting oxygen compositional roughening reduces the overall coordination for Sr and Ti at the interface. The ion sites with lower oxygen coordination give rise to the components at lower binding energy in $Sr\ 3d$ and $Ti\ 2p$ core levels (Fig. 4(b)-(c) and Fig. 5 (a) and (b)). On the contrary, the coordination for Ca and Cu is enhanced at the interface. Consistently, components at higher binding energy are present in both the $Ca\ 2p$ and $Cu\ 2p$ core levels (Fig.5(c) and (d) and Fig. 6). Our hypothesis on the oxygen redistribution is supported by recent theoretical calculations on $ACuO_2$ IL thin films grown on STO substrate.¹⁰ Indeed, it has been reported that the electrostatic instability induces an atomic reconstruction where the oxygen ions move into the A^{2+} plane, thus giving rise

to chain-type CuO formation at the interface. In all core levels shown in Figs. 4-6 the relative contribution to the HAXPES spectra of the components at higher binding energy increases when the SLs are superconducting, i.e. when the films are grown at high oxygen/ozone pressure. This further demonstrates that those components are associated to the ion sites with higher oxygen coordination. In particular, they represent a clear indication that extra oxygen enters the interfaces.

V. CONCLUSIONS

We have investigated by HAXPES the mechanism of interfacial reconstruction in the recently discovered superconducting CCO/STO SLs. Ideally sharp, stoichiometric interfaces in these SLs would result in a strong polar discontinuity at the interfaces between the two constituent blocks that, in turn, should give rise to a built-in, strongly diverging electrostatic potential. The results presented here show that such a potential is suppressed by a mechanism involving oxygen redistribution in the alkaline earth interface planes. Our results on the band

alignment suggest that band doping cannot occur by direct charge transfer at the interface between CCO and STO. However, the extra oxygen ions, which enter the interface in case of strongly oxidizing growth conditions, preserve the interface charge neutrality by leaving holes in the CuO_2 planes, thus making the cuprate block superconducting. The present study shows that a strong polar discontinuity at the interface can be a key ingredient for the synthesis of novel cuprate HTS heterostructures.

VI. ACKNOWLEDGEMENTS

We acknowledge Robert Johnson and the BMBF for financial support under the contract 05 KS4GU3/1. We would also like to thank the staff of the ESRF for providing the x-ray beam, and Julien Duvernay, Lionel Andr e, and Helena Isern for excellent technical support at the ID32 beamline.

This work was partly supported by the Italian MIUR (Grant No. PRIN-20094W2LAY, "Ordine orbitale e di spin nelle eterostrutture di cuprati e manganiti").

-
- * Electronic address: carmela.aruta@spin.cnr.it
- ¹ H. Y. Hwang, Y. Iwasa, M. Kawasaki, B. Keimer, N. Nagaosa and Y. Tokura, *Nat. Mater.* **11**, 103 (2012)
 - ² G. Balestrino, P.G. Medaglia, P. Orgiani, A. Tebano, C. Aruta, S. Lavanga, and A. A. Varlamov *Phys. Rev. Lett.* **89**, 156402 (2002)
 - ³ P.Orgiani et al. *Phys. Rev. Lett.* **98**, 036401 (2007)
 - ⁴ C. Aruta, G. Ghiringhelli, C. Dallera, F. Fracassi, P. G. Medaglia, A. Tebano, N. B. Brookes, L. Braicovich, and G. Balestrino, *Phys. Rev. B* **78**, 205120 (2008)
 - ⁵ G. Balestrino, S. Martellucci, P. G. Medaglia, A. Paoletti, and G. Petrocelli *Phys. Rev. B* **58**, R8925 (1998)
 - ⁶ A. Gozar, G. Logvenov, L. Fitting Kourkoutis, A. T. Bollinger, L. A. Giannuzzi, D. A. Muller and I. Bozovic, *Nature* **455**, 782 (2008)
 - ⁷ G. Logvenov, A. Gozar, I. Bozovic, *Science* **326**, 699 (2009)
 - ⁸ D. Di Castro, M. Salvato, A. Tebano, D. Innocenti, C. Aruta, W. Prellier, O. I. Lebedev, I. Ottaviani, N. B. Brookes, M. Minola, M. Moretti Sala, C. Mazzoli, P.G. Medaglia, G. Ghiringhelli, L. Braicovich, M. Cirillo, G. Balestrino *Phys. Rev. B* **86**, 134524 (2012)
 - ⁹ Nan Yang, D. Di Castro, C. Aruta, C. Mazzoli, M. Minola, N. Brookes, M. Moretti Sala, W. Prellier, O. I. Lebedev, A. Tebano, and G. Balestrino *J. Appl. Phys.* **112**, 123901 (2012)
 - ¹⁰ Zhicheng Zhong, G. Koster, and Paul J. Kelly, *Phys. Rev. B* **85**, 121411(R) (2012)
 - ¹¹ R. Claessen, M Sing, M Paul, G Berner, A Wetscherek, A Miller and W Drube *New J. Phys.* **11**, 125007 (2009)
 - ¹² A. Ohtomo and H. Y. Hwang *Nature* **427**, 423 (2004)
 - ¹³ N. Nakagawa H. Y. Hwang and D. A. Muller *Nature Materials* **5**, 204 (2006)
 - ¹⁴ H.Y. Hwang, *Science*, **313**, 1895 (2006)
 - ¹⁵ A.S. Kalabukhov et al., *Phys. Rev. Lett.* **103**, 146101 (2009)
 - ¹⁶ S. A. Pauli et al. *Phys. Rev. Lett.* **106**, 036101 (2011)
 - ¹⁷ J. Zegenhagen, B. Detlefs, T.-L. Lee, S. Thiess, H. Isern, L. Petit, L. Andre, J. Roy, Y. Mi, and I. Joumard, *Journal of Electron Spectroscopy and Related Phenomena*, 178-179, 258 (2010)
 - ¹⁸ Michel van Veenendaal *Phys. Rev. B* **74**, 085118 (2006)
 - ¹⁹ K. Okada and A. Kotani *Phys. Rev. B* **52**, 4794 (1995)
 - ²⁰ Alexander V. Naumkin, Anna Kraut-Vass, Stephen W. Gaarenstroom, and Cedric J. Powell, NIST Standard Reference Database 20, Version 4.1 (web version) (<http://srdata.nist.gov/xps/>) 2012.
 - ²¹ S. A. Chambers, T. Droubay, T. C. Kaspar, and M. Gutowski, *Journal of Vacuum Science and Technology B: Microelectronics and Nanometer Structures* **22**, 2205 (2004).
 - ²² L.Quiao, T.C. Droubay, T.C. Kaspar, P.V. Sushko, S.A. Chambers, *Surf. Sci.* **605**, 1381 (2011)
 - ²³ S.Yunoki, A. Moreo, E. Dagotto, S. Okamoto, S. S. Kancharla, A. Fujimori, *Phys. Rev. B* **76**, 064532 (2007)
 - ²⁴ D. Goldschmidt et al. *Phys. Rev. B* **35**, 4360 (1987)
 - ²⁵ Y. Tokura et al. *Phys. Rev. B* **41**, 11657 (1990)
 - ²⁶ J. Lee and A. A. Demkov, *Phys. Rev. B* **78**, 193104 (2008)
 - ²⁷ C. Cen, S. Thiel, G. Hammerl, C. W. Schneider, K. E. Andersen, C. S. Hellberg, J. Mannhart, and J. Levy, *Nature Mater.* **7**, 298 (2008)
 - ²⁸ W. A. Harrison et al., *PRB* **18**, 4402 (1978)
 - ²⁹ P.R. Willmott et al. *Phys. Rev. Lett.* **99**, 155502 (2007)
 - ³⁰ M.A. van Veenendaal, H. Eskes, and G.A. Sawatzky, *Phys. Rev. B* **47**, 11462 (1993)
 - ³¹ M. Taguchi, A. Chainani, N. Kanamura, K. Horiba, Y. Tanaka, M. Yabashi, K. Tamasaku, Y. Nishino, D. Miwa, T. Ishikawa, S. Shin, E. Ikenaga, T. Yokoya, K. Kobayashi, T. Mochiku, K. Hirata, and K. Motoya, *Phys. Rev. B* **71**,

- 155102 (2005)
- ³² M. Taguchi, A. Chainani, K. Horiba, Y. Takata, M. Yabashi, K. Tamasaku, Y. Nishino, D. Miwa, T. Ishikawa, T. Takeuchi, K. Yamamoto, M. Matsunami, S. Shin, T. Yokoya, E. Ikenaga, K. Kobayashi, T. Mochiku, K. Hirata, J. Hori, K. Ishii, F. Nakamura, and T. Suzuki, *Phys. Rev. Lett.* **95**, 177002 (2005)
- ³³ C. Schlueter, P. Orgiani, T.-L. Lee, A. Yu. Petrov, A. Galdi, B. A. Davidson, J. Zegenhagen, and C. Aruta, *Phys. Rev. B* **86**, 155102 (2012)
- ³⁴ G. Panaccione, M. Altarelli, A. Fondacaro, A. Georges, S. Huotari, P. Lacovig, A. Lichtenstein, P. Metcalf, G. Monaco, F. Offi, L. Paolasini, A. Poteryaev, O. Tjernberg, and M. Sacchi *Phys. Rev. Lett.* **97**, 116401 (2006)
- ³⁵ M. Minola, D. Di Castro, L. Braicovich, N. B. Brookes, D. Innocenti, M. Moretti Sala, A. Tebano, G. Balestrino, and G. Ghiringhelli *Phys. Rev. B* **85**, 235138 (2012)